

The chirality of ciliary beats

A Hilfinger¹ and F Jülicher

Max Planck Institute for the Physics of Complex Systems, Nöthnitzer Str. 38, 01187 Dresden, Germany

E-mail: julicher@pks.mpg.de

Received 21 December 2007


Accepted for publication 25 February 2008

Published 18 March 2008

Online at stacks.iop.org/PhysBio/5/016003

Abstract

Many eukaryotic cells possess cilia which are motile, whip-like appendages that can oscillate and thereby induce motion and fluid flows. These organelles contain a highly conserved structure called the axoneme, whose characteristic architecture is based on a cylindrical arrangement of nine doublets of microtubules. Complex bending waves emerge from the interplay of active internal forces generated by dynein motor proteins within the structure. These bending waves are typically chiral and often exhibit a sense of rotation. In order to study how the shape of the beat emerges from the axonemal structure, we present a three-dimensional description of ciliary dynamics based on the self-organization of dynein motors and microtubules. Taking into account both bending and twisting of the cilium, we determine self-organized beating patterns and find that modes with both a clockwise and anticlockwise sense of rotation exist. Because of the axonemal chirality, only one of these modes is selected dynamically for given parameter values and properties of dynein motors. This physical mechanism, which underlies the selection of a beating pattern with specific sense of rotation, triggers the breaking of the left–right symmetry of developing embryos which is induced by asymmetric fluid flows that are generated by rotating cilia.

 This article features online multimedia enhancements

1. Introduction

The generation of directed motion on the level of single cells is in many cases achieved through the regular beating of whip-like appendages called cilia or flagella [1]. Such actively bending filaments emerged early in evolution, with a wide range of different eukaryotic organisms possessing cilia and flagella. (Note that many bacteria possess passive, whip-like structures which are of fundamentally different morphology but are also termed flagella.) Eukaryotic cilia and flagella are motile organelles characterized by a common structure called the axoneme, which consists of a regular cylindrical arrangement of elastic filaments of the cytoskeleton, called microtubules, crosslinked in a chiral fashion by motor proteins, called dyneins (see figure 1) [2, 3]. In the axoneme the action of crosslinking motor proteins—consuming the chemical fuel adenosinetriphosphate (ATP)—generates internal stresses which induce locally a relative sliding of microtubules [4, 5]. This relative sliding in turn leads to a bending and twisting of the elastic axonemal structure.

¹ Present address: Department of Systems Biology, Harvard University, 200 Longwood Ave, Boston, MA 02115, USA.

The motility of cilia not only drives the swimming of many single-celled eukaryotic organisms such as protists and spermatozoa [6], but also generates fluid flows relative to cellular surfaces. A prominent example is the vertebrate trachea, in which the collective beat pattern of a large number of cilia induces an upward flow of mucus that forms an important defence mechanism against infections [7]. Fluid flows generated by beating cilia also play an important role during the embryonic development: after the head–tail (anterior–posterior) and the front–back (ventral–dorsal) asymmetries of the developing embryo are established, the final breaking of the left–right symmetry plane requires a chiral process. For many vertebrate species, it has been shown that the left–right symmetry is broken by a chiral fluid flow in a leftward direction, generated by cilia tilted towards the posterior and beating in a clockwise twirling manner [8–11]. (Clockwise when viewed from the distal end towards the base of the cilium. This convention of clockwise and anticlockwise will be used throughout this paper.) Hence, the sense of ciliary rotation determines the direction of the fluid flow which in turn is responsible for determining the left and right sides of the embryo. It has therefore been suggested that the chirality of

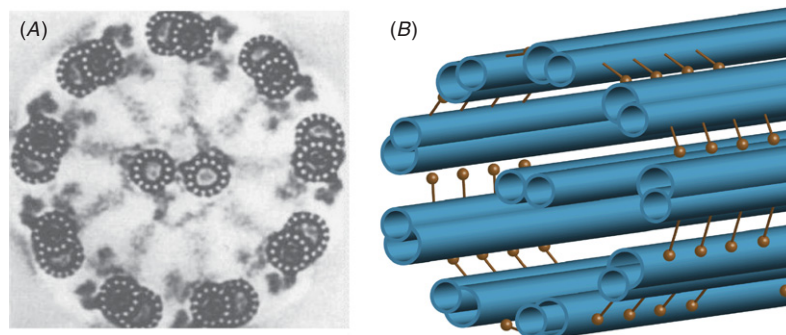


Figure 1. Structure of the axoneme of motile cilia. (A) A computer-enhanced electron micrograph of a cross section displaying the characteristic 9 + 2 arrangement of microtubules (as seen from the basal end). Reprinted from [2]. (B) Schematic illustration of the three-dimensional axonemal geometry indicating the position of molecular motors and microtubule doublets.

the ciliary structure generates the left–right asymmetry of the embryo, by imposing on the ciliary beat patterns a clockwise sense of rotation [12]. However, how the chirality of the axoneme which determines the sense of rotation of twirling beats is not understood.

Periodic and wave-like beating patterns of cilia and flagella are thought to emerge by self-organization from the physical interactions between a large number of motor proteins and the elastic microtubules held together by structural elements such as elastic nexin links. Such self-organized beating could occur in different ways [13–19]. Recent evidence from planar beat patterns of beating bull sperm supports the idea that motor activity is regulated by axonemal sliding and that co-operative behaviour of many motors generate axonemal oscillations [19].

In order to study the shapes and symmetries of helical and rotating beating patterns, we develop a three-dimensional description of axonemal dynamics which generalizes earlier studies of self-organized beating and takes into account both bending and twisting deformations. Our study differs from the existing work for which the shape of the beat was determined numerically in situations where the properties of the spatio-temporal patterns of motor activity were prescribed [20, 21] or determined by a curvature control mechanism [17].

In our description, both the beat pattern as well as the patterns of motor activation emerge from molecular properties of motors and other structural elements as well as their interactions. In a previous study, self-organized axonemal beat patterns were obtained numerically for a model of axonemal dynamics, incorporating a sliding control mechanism similar to that presented in this paper [22]. Here, we perform an analytical study of linearly unstable modes. This enables us to clarify the effects of axonemal chirality on the shapes and symmetries of helical and twirling beat patterns that result from self-organization of motors in the axoneme. The structural chirality of the axoneme leads to an average twist which is the origin of the chirality of the beat pattern. We determine analytically the modes that become unstable when the system approaches an oscillating instability and find that in general both clockwise and anticlockwise modes exist. Which mode is dynamically selected at the instability depends on biophysical parameters characterizing the molecular properties of individual dynein motors.

2. Material reference frame

2.1. Axonemal geometry

The geometry of the axoneme can be characterized by the ensemble of space curves describing the shapes of the microtubule doublets in the axoneme. Given that the axonemal radius a is approximately constant, we can represent the axoneme by a cylindrical surface. Using a material reference frame, this surface can be described by the following two-dimensional parametrization:

$$\mathbf{R}(s, \phi) = \mathbf{r}(s) + a\mathbf{e}_1(s) \cos \phi + a\mathbf{e}_2(s) \sin \phi, \quad (1)$$

where $\mathbf{r}(s)$ is the centre line of the curved cylinder, and ϕ is the angular position of a point on the cylinder. The centre line is parametrized by its arc length s , measured from the base with $0 \leq s \leq L$ where L is the axonemal length. We have introduced the right-handed orthonormal material reference frame $\mathbf{e}_i(s)$, where $\mathbf{e}_3 \equiv \partial\mathbf{r}/\partial s$ is the tangent vector along the centre line. The unit vector \mathbf{e}_1 is perpendicular to \mathbf{e}_3 and identifies the position of a specific microtubule with respect to the centre line. The right-handed reference frame is completed by the unit vector \mathbf{e}_2 normal to the others, see figure 2(A). The shapes of peripheral microtubule doublets correspond to the space curves $\mathbf{R}(s, \phi_n)$, with $\phi_n = 2\pi n/9$ for $n = 0, \dots, 8$ [23] (see figure 2(B)).

The geometry of axonemal deformations is characterized by the dependence of the material reference frame $\mathbf{e}_i(s)$ on the arc length s . This representation describes the larger scale deformations of the structure ignoring details on the small scales such as the twist of individual microtubule doublets. The infinitesimal rotation of this set of unit vectors along the central line is described by

$$\frac{d\mathbf{e}_i}{ds} = \boldsymbol{\Omega} \times \mathbf{e}_i, \quad (2)$$

where the vector $\boldsymbol{\Omega} = \sum_i \Omega_i \mathbf{e}_i$ can be expressed with respect to the material frame. The quantities $\Omega_1(s)$ and $\Omega_2(s)$ then characterize the local curvature of the axoneme, while $\Omega_3(s)$ is the twist density.

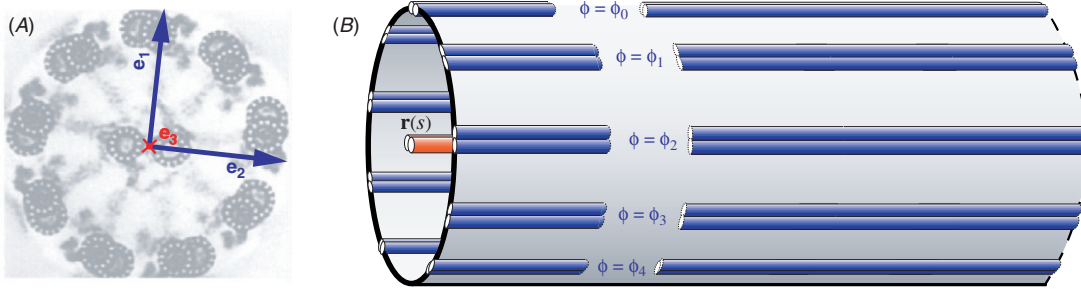


Figure 2. Material reference frame used to describe axonemal deformations. (A) Axonemal cross-section with orthonormal unit vectors \mathbf{e}_1 and \mathbf{e}_2 with the former describing the position of a specific microtubule doublet relative to the centre. The unit vector \mathbf{e}_3 is the tangent to the centre line and points into the plane from the base to the distal end. Edited from [2]. (B) The microtubule doublets define a cylindrical surface. Indicated are the central line $\mathbf{r}(s)$ for a straight axoneme together with lines of constant angle for $\phi_n = 2\pi n/9$ in the material reference frame. These lines describe the shapes of the nine peripheral microtubule doublets.

2.2. Infinitesimal variations of the shape

In order to understand how changes in axonemal shape are related to changes of the material reference frame, we consider infinitesimal variations $\delta\mathbf{r}$ of the centre line and of the twist angle $\delta\vartheta = \mathbf{e}_2 \cdot \delta\mathbf{e}_1$, for which changes of the vectors \mathbf{e}_i obey

$$\begin{aligned}\delta\mathbf{e}_1 &= \delta\vartheta \mathbf{e}_2 - (\mathbf{e}_1 \cdot \partial_s(\delta\mathbf{r}))\mathbf{e}_3 \\ \delta\mathbf{e}_2 &= -\delta\vartheta \mathbf{e}_1 - (\mathbf{e}_2 \cdot \partial_s(\delta\mathbf{r}))\mathbf{e}_3 \\ \delta\mathbf{e}_3 &= \partial_s(\delta\mathbf{r}) - (\mathbf{e}_3 \cdot \partial_s(\delta\mathbf{r}))\mathbf{e}_3.\end{aligned}$$

Note that under the above variations the arc length changes according to $\delta(ds) = (\mathbf{e}_3 \cdot \partial_s(\delta\mathbf{r})) ds$. The corresponding variations of the curvatures and the twist density are given by

$$\begin{aligned}\delta\Omega_1 &= \delta\vartheta \Omega_2 - \mathbf{e}_2 \cdot \partial_s^2(\delta\mathbf{r}) - 2\Omega_1 \mathbf{e}_3 \cdot \partial_s(\delta\mathbf{r}) \\ \delta\Omega_2 &= -\delta\vartheta \Omega_1 + \mathbf{e}_1 \cdot \partial_s^2(\delta\mathbf{r}) - 2\Omega_2 \mathbf{e}_3 \cdot \partial_s(\delta\mathbf{r}) \\ \delta\Omega_3 &= \partial_s(\delta\vartheta) + (\Omega_1 \mathbf{e}_1 + \Omega_2 \mathbf{e}_2 - \Omega_3 \mathbf{e}_3) \cdot \partial_s(\delta\mathbf{r}).\end{aligned}\quad (3)$$

These geometric relations define shape changes of the cylindrical surface in a material reference frame and have been derived previously in [24–27].

3. Energies, forces and moments

3.1. Bending and twisting

Ignoring details on small scales, the elastic properties of the ensemble of microtubule doublets in the axoneme are described by a coarse-grained elastic energy which depends on the local curvatures and the twist density of the axonemal cylinder:

$$E = \int_0^L ds \left\{ \frac{\kappa_1}{2} \Omega_1(s)^2 + \frac{\kappa_2}{2} \Omega_2(s)^2 + \frac{\kappa_3}{2} \Omega_3(s)^2 \right\}, \quad (4)$$

where we have introduced the bending moduli κ_1 and κ_2 as well as a twist modulus κ_3 . Note that this energy does not include the elasticity of elements connecting the microtubule doublets such as nexin links. The effects of elastic elements in the axonemal structure will be combined with the description of motors which are also crosslinkers between microtubule doublets, however with active properties. Note also that we have neglected terms which could couple

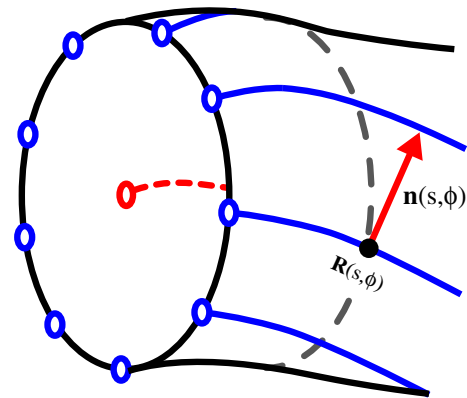


Figure 3. Illustrating the direction $\mathbf{n}(s, \phi)$ that is orthogonal to $\partial_s \mathbf{R}(s, \phi)$ and tangential to the axonemal surface at $\mathbf{R}(s, \phi)$. The grey dashed line indicates the circle of constant ϕ .

twisting and bending because the dominant coupling of twist and bending is introduced by active elements. More general energy functionals for filament bundles have been discussed in [28, 29]. Starting from the energy (4), we can derive dynamic equations which balance elastic, dissipative and active forces which act inside and on the axoneme.

3.2. Relative microtubule sliding and work of internal forces

If the axoneme is bent and twisted, at any given point along the axoneme characterized by the arc length s two adjacent microtubule doublets n and $n+1$ are displaced tangentially relative to each other. We denote this sliding distance $\Delta_{MT}(s, n)$. This sliding distance can be expressed in terms of the deformation of the cylinder by bending and twisting. This relation can be derived by using differential geometry on the surface of the curved cylinder, as follows. The arc length ℓ of a microtubule doublet on the deformed cylinder measured from the base as a function of the arc length s is given by

$$\ell(s, \phi) = \int_0^s |\partial_{s'} \mathbf{R}(s', \phi)| ds'.$$

We define a unit vector $\mathbf{n}(s, \phi)$ that is normal to the microtubule doublet, such that $\mathbf{n} \cdot \partial_s \mathbf{R} = 0$, and tangential

to the cylinder, see figure 3. Introducing the contravariant components of \mathbf{n} , we write $\mathbf{n} = n^s \partial_s \mathbf{R} + n^\phi \partial_\phi \mathbf{R}$, which allows us to define a local displacement density by

$$\Delta(s, \phi) = n^s \partial_s \ell + n^\phi \partial_\phi \ell, \quad (5)$$

where n^s , n^ϕ and $\partial_\phi \ell$, $\partial_s \ell$ are derived explicitly in appendix A. The sliding displacement between neighbouring microtubule doublets can then be defined as

$$\Delta_{\text{MT}}(s, n) = a \int_{\phi_n}^{\phi_{n+1}} \Delta(s, \phi) d\phi. \quad (6)$$

The sliding displacements between adjacent microtubule doublets n and $n + 1$ are driven by relative forces per microtubule length $f_{\text{MT}}(s, n)$ which are exerted by elastic linkers such as nexins (see above) and by dynein motors. Note that the shear force density between microtubules includes friction forces from internal dissipation due to relative sliding. The total work performed by the relative inter-doublet forces f_{MT} is given by

$$W = - \int_0^L ds \sum_{n=0}^8 f_{\text{MT}}(s, n) \Delta_{\text{MT}}(s, n). \quad (7)$$

We therefore define a piecewise constant function $f(s, \phi) = f_{\text{MT}}(s, n)$ for $\phi_n \leq \phi < \phi_{n+1}$ and $n = 0, \dots, 8$, such that the work can be conveniently written as

$$\begin{aligned} W &= -a \int_0^L ds \int_0^{2\pi} d\phi f(s, \phi) \Delta(s, \phi) \\ &= - \int_0^L ds \left[2\pi a \Delta_0 f_0 + \pi a \sum_{k=1}^{\infty} (\Delta_1^{(k)} f_1^{(k)} + \Delta_2^{(k)} f_2^{(k)}) \right], \end{aligned} \quad (8)$$

where we have introduced the discrete Fourier modes in the angle ϕ such that

$$\Delta(s, \phi) = \Delta_0(s) + \sum_{k=1}^{\infty} \Delta_1^{(k)}(s) \cos k\phi + \sum_{k=1}^{\infty} \Delta_2^{(k)}(s) \sin k\phi, \quad (9)$$

and correspondingly for the function $f(s, \phi)$.

In the following, we assume for simplicity, that the motor activity and the resulting sliding displacements are dominated by the modes $\Delta^{(k)}(s)$ and $f^{(k)}(s)$ of low orders k . The modes with $k = 0$ correspond to equal activity independent of ϕ while the mode $k = 1$ implies that sliding and forces alternate on opposite sides of the axoneme. Higher modes correspond to more complex activation patterns around the circumference of the axoneme that could play a role in very complex beating patterns but are not considered here. We therefore focus on Δ_0 , f_0 , $\Delta_{1,2} \equiv \Delta_{1,2}^{(1)}$ and $f_{1,2} \equiv f_{1,2}^{(1)}$ where we have dropped the superscript to keep the notation simple.

For a straight, untwisted axoneme the microtubule arc length ℓ is independent of ϕ , which implies that the sliding density Δ vanishes for a straight, untwisted axoneme. For nonzero curvatures and twist density, the dimensionless sliding density Δ can therefore be expanded in powers of the dimensionless curvatures and twist density $a\Omega_i$. Making use of the results described in appendix A, equation (5) yields to lowest order

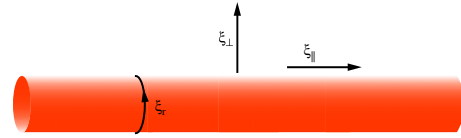


Figure 4. The hydrodynamic effects of the surrounding fluid on the cilium are approximated by local friction coefficients describing perpendicular, longitudinal and rotational motion.

$$\Delta_0(s) = -a\Omega_3(s) \quad (10)$$

$$\Delta_{1,2}(s) = \int_0^s \Omega_{1,2}(s') ds' + \mathcal{O}(a^2 \Omega_i^2). \quad (11)$$

The enthalpy functional $G = E - W$ can now be written as

$$\begin{aligned} G &\simeq E - \int_0^L ds \{ \Lambda(s) + 2\pi a^2 \Omega_3(s) f_0(s) \\ &\quad + a\pi \Omega_1(s) F_1(s) + a\pi \Omega_2(s) F_2(s) \}, \end{aligned} \quad (12)$$

where we have introduced the relative forces

$$F_{1,2}(s) = - \int_s^L f_{1,2}(s') ds'$$

as well as the Lagrange multiplier function $\Lambda(s)$ to impose a constraint of local inextensibility as an approximation for the situation where microtubule stretching can be neglected. Although strictly speaking it is the individual microtubules that are constrained, for realistic values of twist the assumption that the individual microtubules are incompressible is approximated by the condition that the central line of the axonemal cylinder is incompressible. This enthalpy functional is an extension of previous work discussing planar axonemal beat patterns to three dimensions [18, 30]. Alternatively it can also be thought of as a generalization of the dynamics of passive elastic filaments in three dimensions [24] to actively bending filaments.

4. Hydrodynamic forces and mechanical work

The dynamics of the axonemal shape changes are driven by changes of the functional G . Ignoring hydrodynamic interactions, we introduce local hydrodynamic friction coefficients ξ_{\parallel} , ξ_{\perp} and ξ_r for parallel, perpendicular and rotational motions of the cylinder with respect to the fluid (see figure 4). Balancing the axonemal forces $\delta G/\delta \mathbf{r}$ and $\delta G/\delta \vartheta$ with viscous friction forces, we obtain the following equations describing axonemal dynamics

$$\partial_t \mathbf{r} = - \left(\frac{1}{\xi_{\perp}} (\mathbf{e}_1 \otimes \mathbf{e}_1 + \mathbf{e}_2 \otimes \mathbf{e}_2) + \frac{1}{\xi_{\parallel}} \mathbf{e}_3 \otimes \mathbf{e}_3 \right) \cdot \frac{\delta G}{\delta \mathbf{r}} \quad (13)$$

$$\partial_t \vartheta = - \frac{1}{\xi_r} \frac{\delta G}{\delta \vartheta}. \quad (14)$$

In order to find expressions for the axonemal forces $\delta G/\delta \mathbf{r}$, $\delta G/\delta \vartheta$ in the above equations, we make use of the

geometric relations (3). Integration of δG obtained from (12) by parts leads to

$$\begin{aligned} \frac{\delta G}{\delta \mathbf{r}} = & \partial_s [\mathbf{e}_1 (2\pi a^2 f_0 \Omega_1 - a\pi (F_1 \Omega_3 + f_2) \\ & - \Omega_1 \Omega_3 (\kappa_3 - \kappa_1) + \kappa_2 \partial_s \Omega_2) \\ & + \mathbf{e}_2 (2\pi a^2 f_0 \Omega_2 - a\pi (F_2 \Omega_3 - f_1) \\ & - (\kappa_3 - \kappa_2) \Omega_2 \Omega_3 - \kappa_1 \partial_s \Omega_1) - \mathbf{e}_3 \tau] \end{aligned} \quad (15)$$

$$\begin{aligned} \frac{\delta G}{\delta \vartheta} = & a\pi (F_2 \Omega_1 - F_1 \Omega_2) + 2\pi a^2 \partial_s f_0 \\ & - \kappa_3 \partial_s \Omega_3 + (\kappa_1 - \kappa_2) \Omega_1 \Omega_2, \end{aligned} \quad (16)$$

where the tension $\tau(s)$ along the axoneme is given by

$$\tau(s) = -\Lambda - \frac{\kappa_1}{2} \Omega_1^2 - \frac{\kappa_2}{2} \Omega_2^2 - \frac{\kappa_3}{2} \Omega_3^2. \quad (17)$$

The corresponding boundary terms are presented in appendix B.

5. Equations of motion

5.1. Dynamic equations for the shape

The equations of motion for the curvatures and the twist variables Ω_i can be obtained by making use of (3) and the incompressibility constraint

$$\mathbf{e}_3 \cdot \partial_t \partial_s \mathbf{r} = 0, \quad (18)$$

which determines the Lagrange multiplier function $\Lambda(s)$. This leads to

$$\begin{aligned} \partial_t \Omega_1 &= \partial_t \vartheta - \mathbf{e}_2 \cdot \partial_s^2 \partial_t \mathbf{r} \\ \partial_t \Omega_2 &= -\partial_t \vartheta - \mathbf{e}_1 \cdot \partial_s^2 \partial_t \mathbf{r} \\ \partial_t \Omega_3 &= \partial_s \partial_t \vartheta + (\Omega_1 \mathbf{e}_1 + \Omega_2 \mathbf{e}_2) \cdot \partial_s \partial_t \mathbf{r}. \end{aligned} \quad (19)$$

The above expressions together with the force and moment balancing equations (13) and (14) define the nonlinear dynamic equations for the unknowns Ω_i as presented in full in [31].

5.2. Boundary conditions

The equations of motion are complemented by boundary conditions that follow from physical conditions imposed at the ends of the axoneme. The boundary conditions are obtained by matching the external forces and torques with the boundary terms of the variations of G given in appendix B. Here, we assume that the base of the axoneme ($s = 0$) is held fixed, such that it cannot move, tilt or rotate. Assuming that the motion of the distal end ($s = L$) is unconstrained (i.e. that no external torques and forces are applied), we obtain the set of boundary conditions, detailed in table 1.

6. Spontaneous motion

6.1. Force generation by motor proteins

In order to discuss oscillatory beat patterns, we express the time-dependent quantities as a discrete temporal Fourier series,

$$\Omega_i(s, t) = \sum_{n=-\infty}^{\infty} \tilde{\Omega}_i^{(n)}(s) e^{in\omega t}$$

Table 1. Boundary conditions that correspond to a clamped base and a free distal end of the axoneme.

At $s = 0$		
$\partial_t \mathbf{r} = 0$	$\partial_t \partial_s \mathbf{r} = 0$	$\partial_t \vartheta = 0$
At $s = L$		
$\Omega_1 = 0$	$\Omega_2 = 0$	$\tau = 0$
$\partial_s \Omega_1 = \frac{a\pi f_1}{\kappa_1}$	$\partial_s \Omega_2 = \frac{a\pi f_2}{\kappa_2}$	$\Omega_3 = \frac{2\pi a^2}{\kappa_3} f_0$

and similarly for $f(s, t)$, $\Delta(s, t)$, $\tau(s, t)$. In the following, we focus on the fundamental modes with $n = 1$ and drop the superscript, such that $\tilde{\Omega}_i(s)$, $\tilde{\tau}(s)$, $\tilde{\Delta}_i(s)$, $\tilde{f}(s)$ refer to the fundamental Fourier amplitudes of the corresponding time-dependent quantities.

The density of shear forces $f(s, \phi)$ is a result of passive crosslinkers between microtubule doublets as well as the action of dynein motor proteins. For small oscillatory amplitudes and forces, the relation between the fundamental Fourier modes of $f(s, \phi)$ and $\Delta(s, t)$ can be expressed in the form

$$\tilde{f} = \chi \tilde{\Delta} + \mathcal{O}(\tilde{\Delta}^3), \quad (20)$$

where the linear response coefficient χ is a complex number with negative real and imaginary parts. The phase and amplitude of χ results from the combination of passive crosslinkers and collectively operating motors which connect the microtubule doublets [18, 19]. Examples for microscopic mechanisms leading to such a response have been suggested in the form of a relation between motor activity and their sliding rate, alternatively termed ‘shear rate control’ [13, 22] or ‘sliding control’ [18, 19]. The linear response coefficient χ characterizes the mechanical properties of shear forces in the active axoneme. It can be represented in terms of a frequency-dependent negative stiffness $K(\omega)$ and negative friction $\lambda(\omega)$ such that $\chi(\omega) = K(\omega) + i\omega\lambda(\omega)$.

Making use of (11) we can substitute the mechanical relation (20) into the dynamic equations (18) and (19) to obtain a set of nonlinear partial differential equations in Ω_i and τ describing axonemal dynamics, as detailed in [31]. In the following, we discuss spontaneous movements of a cilium in three dimensions that are generated near an oscillatory instability for symmetric bending rigidities ($\kappa \equiv \kappa_1 = \kappa_2$).

6.2. Collective modes

By performing a stability analysis of a straight and stationary axonemal configuration, we identify the time-periodic modes which become unstable to linear order. These modes represent examples of self-organized axonemal beating patterns. Stationary axonemal configurations are obtained if all motors generate the same stationary force density \hat{f}_0 , which leads to a straight, but twisted stationary configuration of the axoneme with $\Omega_{1,2} = 0$ and $\Omega_3 = A \equiv 2\pi a^2 \hat{f}_0 / \kappa_3$. Note that this stationary state is explicitly chiral and differs in a left or a right-handed reference frame. This is because of the chiral structure of the axoneme where motors are oriented in a specific sense of rotation, i.e. the axonemal cross-section does not look the same when viewed from the different ends (see figure 1). In our equations this chirality is apparent in the average twist of the axoneme described by A .

Linearizing the dynamic equations around this state, we find two coupled ordinary differential equations describing the fundamental modes $\tilde{\Omega}_{1,2}(\bar{s})$. They read in dimensionless form

$$\begin{aligned} i\tilde{\omega}\tilde{\Omega}_1 &= -\partial_{\bar{s}}^4\tilde{\Omega}_1 + \bar{\chi}\partial_{\bar{s}}^2\tilde{\Omega}_1 + 4\bar{A}(\partial_{\bar{s}}^3\tilde{\Omega}_2 - \bar{\chi}\partial_{\bar{s}}\tilde{\Omega}_2) \\ i\tilde{\omega}\tilde{\Omega}_2 &= -\partial_{\bar{s}}^4\tilde{\Omega}_2 + \bar{\chi}\partial_{\bar{s}}^2\tilde{\Omega}_2 - 4\bar{A}(\partial_{\bar{s}}^3\tilde{\Omega}_1 - \bar{\chi}\partial_{\bar{s}}\tilde{\Omega}_1), \end{aligned} \quad (21)$$

where we have introduced the rescaled arc length $\bar{s} = s/L$ and the dimensionless parameters $\tilde{\omega} = \omega L^4 \xi_{\perp} / \kappa$, $\bar{A} = AL$, and $\bar{\chi} = \pi a^2 L^2 \chi / \kappa$. To linear order these two modes decouple from the twist dynamics

$$i\tilde{\omega}\bar{\xi}\tilde{\Omega}_3 = (\bar{\kappa}_3 + 2\bar{\chi}\bar{a}^2)\partial_{\bar{s}}^2\tilde{\Omega}_3 \quad (22)$$

where we have introduced $\bar{\xi} = \xi_r / (\xi_{\perp} L^2)$, $\bar{\kappa} = \kappa_3 / \kappa$ and $\bar{a} = a/L$. The boundary conditions complementing equations (21) and (22) are given in appendix B. Bending waves of the axoneme can occur via instabilities of the stationary reference configuration which are described as nontrivial solutions to (21). The resulting spatio-temporal patterns are chiral and exhibit a handedness which will be discussed in the following section. Note that the twist can exhibit separate instabilities described by (22) which are not addressed here. Also note that in the limit of a strongly anisotropic axoneme with bending rigidities $\kappa_2 \gg \kappa_1$ and small twist $\bar{A} = 2\pi a^2 L \hat{f}_0 / \kappa_3 \ll 1$, the dynamics of a cilium is described by equation (21) with small \bar{A} and $\tilde{\Omega}_2$, which corresponds to the equation of motion for planar beat patterns of sperm flagella presented in [19]. Note that if \bar{A} and $\tilde{\Omega}_2$ are small but finite, the beat plane is slightly twisted which leads to a helical swimming trajectory typical for sperm [32].

6.3. Twirling beat patterns

The general solution to the homogeneous boundary value problem (21) is given by

$$\begin{pmatrix} \tilde{\Omega}_1(s) \\ \tilde{\Omega}_2(s) \end{pmatrix} = \sum_{n=1}^{n=4} c_n^+ \begin{pmatrix} 1 \\ i \end{pmatrix} e^{q_n \bar{s}} + c_n^- \begin{pmatrix} 1 \\ -i \end{pmatrix} e^{-q_n \bar{s}}, \quad (23)$$

where q_n are the four complex solutions to the characteristic polynomial

$$q^4 - q^2 \bar{\chi} - 4i\bar{A}(q^3 - q\bar{\chi}) + i\tilde{\omega} = 0. \quad (24)$$

The eight boundary conditions on $\tilde{\Omega}_i$ given in table B1 determine the eight complex coefficients c_n^{\pm} , as detailed in appendix C.

Non-trivial solutions to (23) which satisfy the boundary conditions exist only for a discrete set of specific complex values of $\bar{\chi} = \bar{\chi}_k^{\pm}$, $k = 0, 1, 2, \dots$. For each k , two different solutions exist: for $\bar{\chi}_k^+$ a mode with $c_n^+ \neq 0$, $c_n^- = 0$ and for $\bar{\chi}_k^-$ a mode with $c_n^+ = 0$, $c_n^- \neq 0$. Each of these critical values $\bar{\chi}_k^{\pm}$ thus corresponds to a linearly unstable beating mode of the system.

For given k , the pair of solutions characterized by the values $\bar{\chi}_k^{\pm}$ according to (23) satisfy $\tilde{\Omega}_1(s) = \pm i\tilde{\Omega}_2(s)$. The phase difference of $\pm\pi/2$ between the two fundamental Fourier modes of the curvatures Ω_1 and Ω_2 implies that the time evolution of the shape corresponds to clockwise and anticlockwise helical waves, respectively. This can be shown by defining amplitudes and phases $H^{\pm}(s)$ and $\theta^{\pm}(s)$ of the

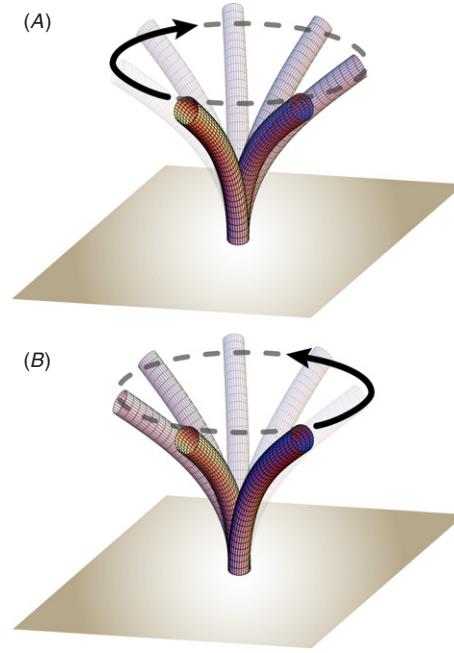


Figure 5. Shape of the linearly unstable modes corresponding to twirling beat patterns in a cilium of length $L = 3 \mu\text{m}$ beating with frequency $\omega/2\pi \approx 10 \text{ Hz}$ given a twist of $\bar{A} = 0.20$. Note that despite the axoneme's chirality, which fixes the sign of the twist \bar{A} , both clockwise as well as anticlockwise helical waves can become unstable. (A) A twirling beat pattern, corresponding to Ω_1^+ exhibiting a clockwise rotation. (B) A twirling beat pattern, corresponding to Ω_1^- exhibiting an anticlockwise rotation. For the purpose of this illustration, the amplitude of the depicted unstable modes was fixed arbitrarily.

curvature waves by $H^{\pm}e^{i\theta^{\pm}} = \sum_n c_n^{\pm} e^{\pm q_n s}$. We can then write

$$\begin{pmatrix} \Omega_1^{\pm}(s, t) \\ \Omega_2^{\pm}(s, t) \end{pmatrix} = \mathbf{M}_{\text{rot}}(\mp\omega t) \begin{pmatrix} H^{\pm}(s) \cos \theta^{\pm}(s) \\ \mp H^{\pm}(s) \sin \theta^{\pm}(s) \end{pmatrix} \quad (25)$$

where $\mathbf{M}_{\text{rot}}(\alpha)$ is the two-dimensional rotation matrix defined in appendix B. The unstable modes with time evolution $\Omega_i^{\pm}(s, t)$ lead to a helical bending wave that corresponds to twirling beat patterns in which the tip of the cilium follows a rotational path in the clockwise (Ω_i^+) or anticlockwise (Ω_i^-) direction (as seen from the distal end). It is important to note that despite the axoneme's chirality, which fixes the sign of the twist, both clockwise as well as anticlockwise helical waves can become unstable.

Examples of such bending modes on the branch of instabilities for $\bar{\chi}_1^{\pm}$ for values of the parameters corresponding to nodal cilia are illustrated in figure 5. Here, we have used $\bar{A} = 0.20$. This is of the order of the twist that can maximally be generated by dynein motors, based on estimates for the time-independent motor activity ($f_0^c \approx 6 \times 10^{-4} \text{ N m}^{-1}$, which corresponds to ten dynein heads per 96 nm structural repeat [33] generating a force of 6 pN) and the twist rigidity of the axoneme ($\kappa_3 \approx 10^{-21} \text{ N m}^2$) [23]. Changing the magnitude of the twist \bar{A} does not qualitatively change our results about the stability of helical ciliary beat patterns. These spontaneously twirling solutions reproduce qualitatively the experimentally

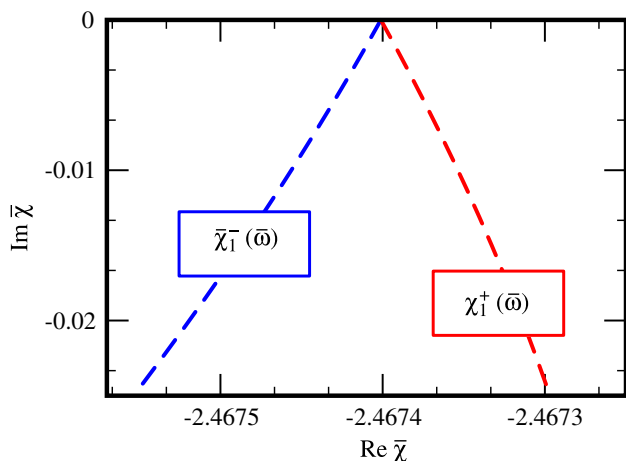


Figure 6. The clockwise twirling modes $\Omega_1^+(s, t)$ and anticlockwise twirling modes $\Omega_1^-(s, t)$ correspond to critical values of $\bar{\chi}(\bar{\omega})$ for which the system of equations has nonzero solutions. Displayed are the leading pair of critical branches $\bar{\chi}_1^\pm(\bar{\omega})$ for $0 \leq \bar{\omega} \leq 0.10$.

observed vortical beat patterns of nodal cilia [10, 11] and other $9 + 0$ monocilia [9].

The critical values of the linear response coefficient $\bar{\chi}$ are functions of the frequency, defining pairs of branches $\bar{\chi}_k^\pm(\bar{\omega})$ that originate from the points $\bar{\chi}_k^\pm(0) = -((2k+1)\pi/2)^2$ on the real axis. The leading pair $\bar{\chi}_1^\pm(\bar{\omega})$ is depicted in figure 6 for small values of $\bar{\omega}$. For completeness the first three pairs of branches are displayed in appendix C for a larger range of $\bar{\omega}$, indicating the structure of instabilities in the space of complex $\bar{\chi}$ values.

6.4. Sense of rotation

Note that the above description of unstable modes is generic insofar as it is independent of the detailed microscopic motor dynamics. Each linear mode corresponds to a given bifurcation frequency, and which frequency (and therefore which mode) becomes unstable is determined by the following microscopic condition: at the instability, the linear response function $\bar{\chi}(\omega)$ matches a critical value $\bar{\chi}(\omega) = \chi_k^\pm(\omega)$, which selects the frequency and the mode that becomes unstable for a given linear response function $\bar{\chi}(\omega)$ of the motor collection within the axoneme. The frequency of the beat at the instability is therefore not generic but depends on the properties of the active motor molecules. Using models for motor co-operativity, one can find explicit expressions for $\bar{\chi}(\omega)$ [18, 19, 34, 35]. A typical example is given by

$$\chi(\omega) = K + i\omega\lambda - \rho k \epsilon \frac{i\omega\bar{\tau} + (\omega\bar{\tau})^2}{1 + (\omega\bar{\tau})^2}, \quad (26)$$

where k is a stiffness of a motor domain, ρ the density of motors along the axoneme, K and λ the internal elasticity and friction associated with microtubule sliding, τ the correlation time of motor attachments and detachments and ϵ denotes a dimensionless control parameter [18, 19]. For such a specific example, we can find the critical values of ϵ for which the modes $\tilde{\Omega}_i^\pm(s)$ become unstable. Using estimates for the values for the microscopic parameters [18, 19], we find that the

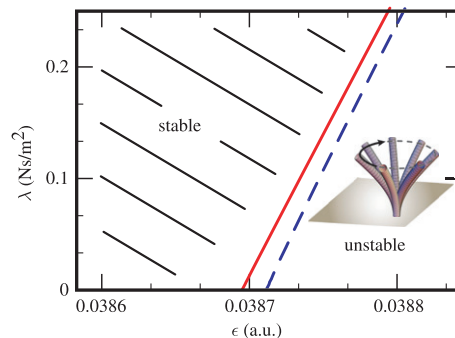


Figure 7. Stability diagram in the (ϵ, λ) plane where ϵ denotes the dimensionless control parameter in arbitrary units and λ is the internal passive sliding resistance λ in the axoneme. Displayed are the lines of instability which correspond to clockwise (solid line, red) and anticlockwise (dashed line, blue) twirling patterns. Parameter values are $L = 3 \times 10^{-6}$ m, $\kappa = 1.7 \times 10^{-21}$ kg m³ s⁻², $\xi_\perp = 2.5 \times 10^{-3}$ kg m⁻¹ s⁻¹, $K = 10^3$ kg m⁻¹, $\tau = 5 \times 10^{-3}$ s, $a = 90 \times 10^{-9}$ m.

clockwise (as seen from the distal end) twirling beat patterns corresponding to $\tilde{\Omega}_1^+(s)$ become unstable first. This is shown in figure 7 where for the purpose of the illustration we present a region of the stability diagram where the two lines of instability can be clearly distinguished. This region corresponds to small values of λ and large values of the bifurcation frequency. As λ increases, the frequency of the bifurcation decreases. Our estimates of the parameter values of cilia correspond to values of $\lambda \simeq 5 \times 10^2$ N s m⁻² for which the frequency is $\omega/2\pi \simeq 10$ Hz.

7. Discussion

The motility of cilia and flagella lies at the heart of many biological processes, relevant to fields as diverse as the swimming of microorganisms, developmental biology and medicine. In this paper, we present a theoretical description of the ciliary dynamics, in which the axoneme is represented by a cylinder, the surface of which can be mapped to the nine circumferential microtubule doublets. Spatio-temporal activation patterns of dynein motors in the axoneme are then described by time-dependent distributions of shear force density on the cylinder surface and induce bending and twisting deformations of the cylinder.

We analysed the dynamics of cilia, neglecting hydrodynamic interactions and considering the simplest case of an axoneme with isotropic bending stiffness ($\kappa_1 = \kappa_2$). We derived equations of motion (21) for the fundamental modes which emerge by self-organization for a given physical feedback between motor activity and relative sliding displacement of microtubule doublets. Our approach allowed us to show analytically that self-organized twirling beat patterns can emerge from a generic feedback between motor activity and local sliding displacement.

Key to the chirality of emergent beat patterns is the fact that motor activity in the axoneme leads to an average twist A as a result of the chiral asymmetry of the axonemal structure. In previous work, it was suggested that this effect is weak

[23]. Here, we have shown that this motor-induced twist is important for the selection of a definite sense of rotation of twirling motion. Note that the average twist A discussed in this work follows directly from the known properties of dynein activity within the axoneme and has a definite sign, unlike the twist introduced in [22].

The general framework we develop here can also be related to planar beat patterns such as those of many sperm. A planar beat can emerge in situations where the bending rigidity is anisotropic such that bending is facilitated in a fixed direction with respect to the material reference frame. This corresponds in our description to a case where the two bending moduli have very different values ($\kappa_2 \gg \kappa_1$). Such a strong bending anisotropy could result from structural constraints which suppress relative sliding of one pair of microtubule doublets [23, 36–39]. If there is no twist in the axoneme, the equations described here approach in this case of strong anisotropy the limit of a two-dimensional planar beat [18]. In this limit, our theory can be directly and quantitatively compared to experimentally observed beat patterns, which provides strong evidence for the sliding control mechanism of motors in sperm [19].

Because of the chiral structure of the axoneme, in general a small twist will occur as a consequence of average motor activity. If the average twist density \bar{A} is small, the beat plane will twist slightly, but the beat pattern look almost planar. This is consistent with the commonly observed helical swimming paths of many sperm with almost planar beat patterns [32, 40].

The equations for linearly unstable modes have two types of helical wave solutions which rotate in either clockwise or anticlockwise direction (see figure 5). Because of the axonemal chirality, modes with one sense of rotation become unstable first and the selected rotating wave has a definite sense of rotation. However, this sense of rotation is selected dynamically and depends on the details of the properties of the feedback which is described by the linear response function $\chi(\omega)$. Therefore, by changing parameter values such as the internal shear resistance or motor properties such as on- and off-rates, the sense of rotation can in principle be inverted even though the structural chirality is not changed. This dynamic selection of asymmetric states is similar in its nature to how the direction of motion of motor proteins along a filament is determined by the spatial asymmetry of the filament. In the case of a motor-filament system, the filament polarity determines the direction of motion of a given motor, but different motors can move in opposite directions because the directionality of motion depends on both structural and kinetic properties of motors and filaments [34, 41, 42].

Analysing a simple model of collective motor action, we find that the clockwise twirling beat patterns become unstable first and thus represent the principal beating mode. This corresponds to the predominantly clockwise twirling beat patterns observed of monocilia lacking the central pair of microtubules (9 + 0 cilia) [9–11]. As mentioned above, interestingly the system can also become unstable with respect to anticlockwise twirling patterns, despite the axoneme's chirality that selects a preferred twist. Note that anticlockwise beat patterns have been reported in a small number of cilia

in mutant (*inv*) mouse embryos [10], and individual cilia in developing rabbit embryos have been observed to infrequently undergo transitions from clockwise to anticlockwise beat patterns and back [43].

8. Conclusion and outlook

During the development of many vertebrate species, groups of cilia on the surface of the embryo rotate in a chiral manner. The sense of rotation of these nodal cilia generates a chiral fluid flow which in turn controls the left–right symmetry breaking of the developing embryo. Therefore, the question of how the sense of rotation of 9 + 0 cilia is selected is fundamentally linked to developmental processes. In the developmental context, many rotating cilia interact hydrodynamically. In this situation, a definite chirality of the net flow emerges from an array of twirling cilia [44–46]. It will be of interest to extend our analysis to include hydrodynamic interactions, by incorporating our description of self-organized three-dimensional axonemal beat patterns into the framework of existing studies on synchronization phenomena in cilia [44, 45, 47].

Our analysis focuses on the lowest order temporal and angular Fourier modes of the beat, which dominate for simple rotating or helical waves. More complex beating patterns that are strongly non-harmonic, such as the complex beating pattern of cilia which generate an active stroke and a recovery stroke near a surface, involve higher order Fourier modes. The same arguments also apply for the angular Fourier modes around the axoneme. While for harmonic helical or rotating modes only the lowest Fourier modes are relevant, higher modes become important for more complex beat patterns. Furthermore for beat patterns with large amplitude, the effect of nonlinearities cannot be neglected.

Previous numerical studies of the nonlinear dynamics of twirling axonemes suggest that clockwise and anticlockwise rotating solutions could coexist for certain parameter values [22]. Such coexistence of modes is a global property of the dynamic system which is not described by a linear stability analysis but in general results from the nature of nonlinearities. In a sliding control model for axonemal oscillations, nonlinearities are expected to be dominated by collective nonlinearities of motors which depend on details of motor properties and their interactions [34]. The role of motor-induced nonlinearities can be studied systematically. For planar sperm beats these and other nonlinearities do not significantly affect the waveform but determine the amplitude of the beat [48].

A numerical study of the full nonlinear equations of ciliary dynamics in three dimensions, including motor-generated nonlinearities, is therefore of interest to describe large amplitude oscillations and the dynamics of higher order modes. Together with our present work, such full simulations of nonlinear axonemal dynamics could in the future clarify the role of nonlinearities for the observation of coexistence of clockwise and anticlockwise rotating patterns in simulations [22].

To make quantitative comparisons between Fourier modes of observed ciliary beat patterns and theoretical ones, similarly to the work on planar beat patterns of bull sperm [19] will be difficult, as improving current light microscopy methods to reach the necessary spatio-temporal resolution would push the available experimental techniques to their limits. However, one of the main predictions of our work is raising the possibility of transitions between clockwise and anticlockwise rotations. We therefore suggest that careful observations of beating nodal cilia should be made in order to study their sense or rotation and switching events between different rotation senses. It would be interesting to do so in varying conditions, for example examining the effect of changes in intracellular salt concentrations, which can affect the motor dynamics and therefore potentially alter the dynamic mode selection.

Recent work has shown that the mechanical properties of the basal connection between microtubules can fundamentally influence the shape of the planar axonemal beat [19]. In the present work describing three-dimensional ciliary beat patterns, we have considered only the simplest case where no sliding exists at the base. Further work will be necessary to examine the effects of elastic and viscous properties of the basal connection varying around the basal circumference of the axoneme. Based on the analysis of planar beat patterns [19] and the observation that ‘the diversity of structural organization of the basal apparatus between different animals is considerable’ [49], we speculate that the properties of structural elements at the base and their spatial organization could control the shape and asymmetry of three-dimensional beat patterns, the sense of rotation and the degree of planarity of initially helical waves.

9. Supplementary material

- *Movie S1.* Animation of a theoretical beat pattern, corresponding to the unstable mode $\Omega_1^+(s, t)$ presented in figure 5(A). (52 KB MOV) stacks.iop.org/PhysBio/5/016003
- *Movie S2.* Animation of a theoretical beat pattern, corresponding to the unstable mode $\Omega_1^-(s, t)$ presented in figure 5(B). (52 KB MOV) stacks.iop.org/PhysBio/5/016003

Acknowledgments

We thank M Blum, J Howard, K Kruse, I H Riedel-Kruse and A Vilfan for many insightful discussions and J Howard for a critical reading of the manuscript.

Appendix A. Differential geometry on the axoneme

In order to determine the partial derivatives $\partial_s \ell$, $\partial_\phi \ell$ and the contravariant components n^s , n^ϕ we make use of

$$\begin{aligned}\partial_\phi \mathbf{R} &= -a\mathbf{e}_1 \sin \phi + a\mathbf{e}_2 \cos \phi \\ \partial_s \mathbf{R} &= -\mathbf{e}_1 a\Omega_3 \sin \phi + \mathbf{e}_2 a\Omega_3 \cos \phi \\ &\quad + \mathbf{e}_3(1 - a(\Omega_2 \cos \phi - \Omega_1 \sin \phi))\end{aligned}$$

$$\begin{aligned}\partial_s \partial_\phi \mathbf{R} &= -a\Omega_3(\mathbf{e}_1 \cos \phi + \mathbf{e}_2 \sin \phi) \\ &\quad + a\mathbf{e}_3(\Omega_1 \cos \phi + \Omega_2 \sin \phi) \\ \partial_s \mathbf{R} \cdot \partial_s \mathbf{R} &= 1 - 2a(\Omega_2 \cos \phi - \Omega_1 \sin \phi) \\ &\quad + a^2(\Omega_3^2 + (\Omega_2 \cos \phi - \Omega_1 \sin \phi)^2) \\ \partial_\phi \mathbf{R} \cdot \partial_\phi \mathbf{R} &= a^2 \\ \partial_s \mathbf{R} \cdot \partial_\phi \mathbf{R} &= a^2\Omega_3 \\ \partial_s \mathbf{R} \cdot \partial_s \partial_\phi \mathbf{R} &= a(1 - a(\Omega_2 \cos \phi - \Omega_1 \sin \phi)) \\ &\quad \times (\Omega_1 \cos \phi + \Omega_2 \sin \phi).\end{aligned}$$

These quantities then straightforwardly define the partial derivatives

$$\partial_s \ell = \sqrt{\partial_s \mathbf{R} \cdot \partial_s \mathbf{R}} \quad (\text{A.1})$$

$$\partial_\phi \ell = \int_0^s ds' \frac{\partial_s \mathbf{R} \cdot \partial_s \partial_\phi \mathbf{R}}{\sqrt{\partial_s \mathbf{R} \cdot \partial_s \mathbf{R}}}. \quad (\text{A.2})$$

The contravariant components follow from the orthonormality condition for \mathbf{n} and can be written in terms of the above quantities as

$$n^s = -\frac{1}{|\partial_s \mathbf{R}|} \frac{\partial_s \mathbf{R} \cdot \partial_\phi \mathbf{R}}{\sqrt{|\partial_s \mathbf{R}|^2 |\partial_\phi \mathbf{R}|^2 - (\partial_s \mathbf{R} \cdot \partial_\phi \mathbf{R})^2}} \quad (\text{A.3})$$

$$n^\phi = \frac{|\partial_s \mathbf{R}|}{\sqrt{|\partial_s \mathbf{R}|^2 |\partial_\phi \mathbf{R}|^2 - (\partial_s \mathbf{R} \cdot \partial_\phi \mathbf{R})^2}}. \quad (\text{A.4})$$

Equations (A.1)–(A.4) define the vector \mathbf{n} which characterizes the direction from which motors attach to microtubule doublets in the axoneme (see figures 1 and 3). The sign of \mathbf{n} and of the sliding displacement density Δ given by (5) corresponds to the chiral structure of the axoneme as follows: choosing the sign of f such that active motors generate positive force density f , the sliding displacement between microtubule doublets Δ is negative while the resulting twist density Ω_3 and the work W are positive. This corresponds to the axonemal situation in which the peripheral microtubule doublets describe a right-handed helix around the central axis, and where the minus end directed motor proteins move towards the base, causing relative sliding in the chiral arrangement shown in figure 1.

Appendix B. Boundary terms

B.1. Boundary forces and torques

The boundary terms generated by the partial integration of the enthalpy functional (12) correspond to the forces and torques at the ends of the axoneme and are given by

$$\begin{aligned}\left[\frac{\delta G}{\delta \mathbf{r}} \cdot (\delta \mathbf{r}) + (\kappa_3 \Omega_3 - 2\pi a^2 f_0)(\delta \vartheta) + (\mathbf{e}_1(\kappa_2 \Omega_2 - \pi a F_2) \right. \\ \left. - \mathbf{e}_2(\kappa_1 \Omega_1 - \pi a F_1)) \cdot (\delta \partial_s \mathbf{r}) \right]_{s=0}^{s=L}.\end{aligned}$$

B.2. Linear modes boundary conditions

The boundary conditions that complement the dynamic equations (21) and define the linearly unstable bending modes are summarized in table B1.

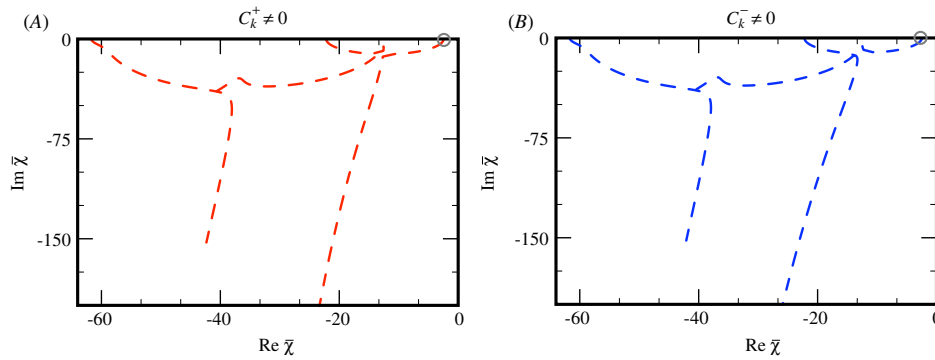


Figure B1. The conditions for nonzero solutions to exist are $\det Q_{mn}^{(+)}(\bar{\chi}, \bar{\omega}) = 0$ or $\det Q_{mn}^{(-)}(\bar{\chi}, \bar{\omega}) = 0$, and lead to a discrete spectrum of values for $\bar{\chi}(\bar{\omega})$ for which the system of equations has nonzero solutions. Here we show the leading branches of critical values $\bar{\chi}_k^{\pm}$ for $k = 0, 1, 2$ starting from $\bar{\omega} = 0$ on the real axis. The red dashed lines in (A) correspond to $\det Q_{mn}^{(+)}(\bar{\chi}, \bar{\omega}) = 0$ and $\Omega_1^+(s, t)$ solutions, while the blue dashed lines in (B) correspond to $\det Q_{mn}^{(-)}(\bar{\chi}, \bar{\omega}) = 0$ and $\Omega_1^-(s, t)$ solutions. The grey circles indicate the region magnified in figure 6.

Table B1. Boundary conditions satisfied by the linearly unstable bending modes.

At $\bar{s} = 0$	at $\bar{s} = 1$
$\partial_{\bar{s}}^2 \tilde{\Omega}_1 = \bar{\chi} \tilde{\Omega}_1 + 2\bar{A} \partial_{\bar{s}} \tilde{\Omega}_2$	$\tilde{\Omega}_1 = 0$
$\partial_{\bar{s}}^2 \tilde{\Omega}_2 = \bar{\chi} \tilde{\Omega}_2 - 2\bar{A} \partial_{\bar{s}} \tilde{\Omega}_1$	$\tilde{\Omega}_2 = 0$
$\partial_{\bar{s}}^3 \tilde{\Omega}_1 = \bar{\chi} \partial_{\bar{s}} \tilde{\Omega}_1 + 3\bar{A}(\partial_{\bar{s}}^2 \tilde{\Omega}_2 - \bar{\chi} \tilde{\Omega}_2)$	$\partial_{\bar{s}} \tilde{\Omega}_1 = \bar{\chi} \int_0^1 \tilde{\Omega}_1(\bar{s}) d\bar{s}$
$\partial_{\bar{s}}^3 \tilde{\Omega}_2 = \bar{\chi} \partial_{\bar{s}} \tilde{\Omega}_2 - 3\bar{A}(\partial_{\bar{s}}^2 \tilde{\Omega}_1 - \bar{\chi} \tilde{\Omega}_1)$	$\partial_{\bar{s}} \tilde{\Omega}_2 = \bar{\chi} \int_0^1 \tilde{\Omega}_2(\bar{s}) d\bar{s}$

Table B2. Boundary conditions satisfied by the linearly unstable twist modes.

At $\bar{s} = 0$	at $\bar{s} = 1$
$(\bar{\kappa}_3 + 2\bar{\chi} \bar{a}^2) \partial_{\bar{s}} \tilde{\Omega}_3 = 0$	$\tilde{\Omega}_3 = 0$

B.3. Twist instability

Independent of the bending instabilities the twist density Ω_3 can become unstable, as defined by the boundary conditions of table B2, complementing equation (22).

Appendix C. Unstable modes

C.1. Boundary value problem

The dynamics equations (21) together with the boundary conditions summarized in table B1 lead to a set of two uncoupled matrix equations of the form $Q_{mn}^{(+)}(\bar{\chi}, \bar{\omega}) c_n^+ = 0$ and $Q_{mn}^{(-)}(\bar{\chi}, \bar{\omega}) c_n^- = 0$, where the matrices $Q_{mn}^{(\pm)}(\bar{\chi}, \bar{\omega})$ are given by

$$\begin{aligned}
 Q_{1,n}^{(+)} &= \bar{\chi} - q_n^2 + 2Ai q_n \\
 Q_{2,n}^{(+)} &= \bar{\chi} q_n - q_n^3 + 3Ai(q_n^2 - \bar{\chi}) \\
 Q_{3,n}^{(+)} &= e^{q_n} \\
 Q_{4,n}^{(+)} &= \frac{\bar{\chi}}{q_n} (e^{q_n} - 1) - q_n e^{q_n} + Ai e^{q_n} \\
 Q_{1,n}^{(-)} &= \bar{\chi} - q_n^2 + 2Ai q_n \\
 Q_{2,n}^{(-)} &= \bar{\chi} q_n - q_n^3 + 3Ai(q_n^2 - \bar{\chi})
 \end{aligned}$$

$$Q_{3,n}^{(-)} = e^{-q_n}$$

$$Q_{4,n}^{(-)} = \frac{\bar{\chi}}{q_n} (e^{-q_n} - 1) - q_n e^{-q_n} + Ai e^{-q_n}.$$

where $n = 1, 2, 3, 4$ and $q_n = q_n(\bar{\chi}, \bar{\omega})$ are the four complex roots of the characteristic polynomial (24). For nonzero solutions to exist, one of the matrices $Q_{mn}^{(\pm)}$ has to be singular, which leads to a discrete spectrum of $\bar{\chi}_k^{\pm}$ values as illustrated in figure B1.

C.2. Rotation matrix

The two-dimensional rotation matrix is defined as

$$\mathbf{M}_{\text{rot}}(\alpha) = \begin{pmatrix} \cos \alpha & -\sin \alpha \\ \sin \alpha & \cos \alpha \end{pmatrix}.$$

Glossary

- **Microtubules.** Cytoskeletal filaments with a diameter of about 25 nm. They behave as elastic rods and have a persistence length of several millimetres. Their structural polarity provides a directionality for motor proteins.
- **Dynein.** Molecular motor that converts chemical energy in the form of ATP into work. It generates motion along microtubules in the direction towards the minus end.
- **Axoneme.** Evolutionary highly conserved structure that consists of nine cylindrically arranged microtubule doublets, linked by dynein motors and passive elastic elements. Constitutes the motile element of cilia and flagella.
- **Sliding control.** General mechanism by which the activity of motors within the axoneme is related to the forces exerted by the motors due to the local shear-rate.
- **Nodal cilia.** Rotating cilia that generate a directed fluid flow during embryonic development in many vertebrate species and thereby break the left–right symmetry axis. Due to their chiral structure and their ability to break the left–right symmetry, prime candidates to encode the third body axis with respect to the earlier established head–tail and front–back body axes.

- *Clockwise/anticlockwise*. In this paper, all beat patterns and their sense of rotation are described when viewed from the distal end of the axoneme towards the base.

References

- [1] Gibbons I R 1981 Cilia and flagella of eukaryotes *J. Cell Biol.* **91** 107s–124s
- [2] Afzelius B A, Dallai R, Lanzavecchia S and Belloni P L 1995 Flagellar structure in normal human spermatozoa and in spermatozoa that lack dynein arms *Tissue Cell* **27** 241–7
- [3] Nicastro D, Schwartz C, Pierson J, Gaudette R, Porter M E and McIntosh J R 2006 The molecular architecture of axonemes revealed by cryoelectron tomography *Science* **313** 944–8
- [4] Satir P 1965 Studies on cilia: II. Examination of the distal region of the ciliary shaft and the role of the filaments in motility *J. Cell Biol.* **26** 805–34
- [5] Gibbons I R and Rowe A J 1965 Dynein—a protein with adenosine triphosphatase activity from cilia *Science* **149** 424–6
- [6] Bray D 2001 *Cell Movements: From Molecules to Motility 2nd edn* (New York: Garland)
- [7] Knowles M R and Boucher R C 2002 Mucus clearance as a primary innate defense mechanism for mammalian airways *J. Clin. Invest.* **109** 571–7
- [8] Nonaka S, Tanaka Y, Okada Y, Takeda S, Harada A, Kanai Y, Kido M and Hirokawa N 1998 Randomization of left–right asymmetry due to loss of nodal cilia generating leftward flow of extraembryonic fluid in mice lacking KIF3B motor protein *Cell* **95** 829
- [9] Kramer-Zucker A G, Olale F, Haycraft C J, Yoder B K, Schier A F and Drummond I A 2005 Cilia-driven fluid flow in the zebrafish pronephros, brain and Kupffer's vesicle is required for normal organogenesis *Development* **132** 1907–21
- [10] Okada Y, Takeda S, Tanaka Y, Belmonte J and Hirokawa N 2005 Mechanism of nodal flow: a conserved symmetry breaking event in left–right axis determination *Cell* **121** 633
- [11] Schweickert A, Weber T, Beyer T, Vick P, Bogusch S, Feistel K and Blum M 2007 Cilia-driven leftward flow determines laterality in *Xenopus* *Curr. Biol.* **17** 60–6
- [12] Wood W B 2005 The left–right polarity puzzle: determining embryonic handedness *PLoS Biol.* **3** e292
- [13] Brokaw C J 1975 Molecular mechanism for oscillation in flagella and muscle *Proc. Natl Acad. Sci. USA* **72** 3102–6
- [14] Lindemann C B 1994 A geometric clutch hypothesis to explain oscillations of the axoneme of cilia and flagella *J. Theor. Biol.* **168** 175–89
- [15] Lindemann C B 1994 A model of flagellar and ciliary functioning which uses the forces transverse to the axoneme as the regulator of dynein activation *Cell Motil Cytoskel* **29** 141–54
- [16] Brokaw C J and Luck D J 1985 Bending patterns of *Chlamydomonas* flagella: III. A radial spoke head deficient mutant and a central pair deficient mutant *Cell Motil Cytoskel* **5** 195–208
- [17] Brokaw C J 2002 Computer simulation of flagellar movement: VIII. Coordination of dynein by local curvature control can generate helical bending waves *Cell Motil Cytoskel* **53** 103–24
- [18] Camalet S and Jülicher F 2000 Generic aspects of axonemal beating *New J. Phys.* **2** 1–23
- [19] Riedel-Kruse I H, Hilfinger A, Howard J and Jülicher F 2007 How molecular motors shape the flagellar beat *HFSP J.* **1** 192–208
- [20] Gueron S and Levit-Gurevich K 1998 Computation of the internal forces in cilia: application to ciliary motion, the effects of viscosity, and cilia interactions *Biophys. J.* **74** 1658–76
- [21] Gueron S and Levit-Gurevich K 2001 A three-dimensional model for ciliary motion based on the internal 9 + 2 structure *Proc. R. Soc. B* **268** 599–607
- [22] Brokaw C J 2005 Computer simulation of flagellar movement: IX. Oscillation and symmetry breaking in a model for short flagella and nodal cilia *Cell Motil Cytoskel* **60** 35–47
- [23] Hines M and Blum J J 1983 Three-dimensional mechanics of eukaryotic flagella *Biophys. J.* **41** 67–79
- [24] Goldstein R E, Powers T R and Wiggins C H 1998 Viscous nonlinear dynamics of twist and writhe *Phys. Rev. Lett.* **80** 5232–5
- [25] Wiggins C H, Rivelino D, Ott A and Goldstein R E 1998 Trapping and wiggling: elastohydrodynamics of driven microfilaments *Biophys. J.* **74** 1043–60
- [26] Wolgemuth C W, Powers T R and Goldstein R E 2000 Twirling and whirling: viscous dynamics of rotating elastic filaments *Phys. Rev. Lett.* **84** 1623–6
- [27] Wolgemuth C W, Goldstein R E and Powers T R 2004 Dynamic supercoiling bifurcations of growing elastic filaments *Physica D* **190** 266–89
- [28] Srigiriraju S V and Powers T R 2005 Continuum model for polymorphism of bacterial flagella *Phys. Rev. Lett.* **94** 248101
- [29] Srigiriraju S V and Powers T R 2006 Model for polymorphic transitions in bacterial flagella *Phys. Rev. E* **73** 011902
- [30] Camalet S, Jülicher F and Prost J 1999 Self-organized beating and swimming of internally driven filaments *Phys. Rev. Lett.* **82** 1590–3
- [31] Hilfinger A 2006 Dynamics of cilia and flagella *Doctoral Dissertation TU Dresden*
- [32] Friedrich B M and Jülicher F 2007 Chemotaxis of sperm cells *Proc. Natl Acad. Sci. USA* **104** 13256–61
- [33] Porter M E and Sale W S 2000 The 9 + 2 axoneme anchors multiple inner arm dyneins and a network of kinases and phosphatases that control motility *J. Cell Biol.* **151** 37F–42
- [34] Jülicher F and Prost J 1997 Spontaneous oscillations of collective molecular motors *Phys. Rev. Lett.* **78** 4510–3
- [35] Pecreaux J, Roper J C, Kruse K, Jülicher F, Hyman A A, Grill S W and Howard J 2006 Spindle oscillations during asymmetric cell division require a threshold number of active cortical force generators *Curr. Biol.* **16** 2111–22
- [36] Afzelius B 1959 Electron microscopy of the sperm tail—results obtained with a new fixative *J. Biophys. Biochem. Cy.* **5** 269–78
- [37] Olson G E and Linck R W 1977 Observations of the structural components of flagellar axonemes and central pair microtubules from rat sperm *J. Ultrastruct. Res.* **61** 21–43
- [38] Lindemann C B, Orlando A and Kanous K S 1992 The flagellar beat of rat sperm is organized by the interaction of two functionally distinct populations of dynein bridges with a stable central axonemal partition *J. Cell Sci.* **102** 249–60
- [39] Si Y and Okuno M 1995 Extrusion of microtubule doublet outer dense fibers 5–6 associating with fibrous sheath sliding in mouse sperm flagella *J. Exp. Zool.* **273** 355–62
- [40] Gray J and Hancock G J 1955 The propulsion of sea-urchin spermatozoa *J. Exp. Biol.* **32** 802–14
- [41] Howard J 2001 *Mechanics of Motor Proteins and the Cytoskeleton* (Sunderland, MA: Sinauer Associates, Publishers)
- [42] Endow S A and Higuchi H 2000 A mutant of the motor protein kinesin that moves in both directions on microtubules *Nature* **406** 913–6
- [43] Blum M 2007 Private communication

- [44] Vilfan A and Jülicher F 2006 Hydrodynamic flow patterns and synchronization of beating cilia *Phys. Rev. Lett.* **96** 058102
- [45] Guirao B and Joanny J F 2007 Spontaneous creation of macroscopic flow and metachronal waves in an array of cilia *Biophys. J.* **92** 1900–17
- [46] Riedel I H, Kruse K and Howard J 2005 A self-organized vortex array of hydrodynamically entrained sperm cells *Science* **309** 300–3
- [47] Gueron S, Levit-Gurevich K, Liron N and Blum J J 1997 Cilia internal mechanism and metachronal coordination as the result of hydrodynamical coupling *Proc. Natl Acad. Sci. USA* **94** 6001–6
- [48] Hilfinger A, Chattopadhyay A K and Jülicher F Nonlinear dynamics of cilia and flagella, in preparation
- [49] Holley M C 1985 Adaptation of a ciliary basal apparatus to cell shape changes in a contractile epithelium *Tissue Cell* **17** 321–34